

# Exploring the Physical Limits of Axial Magnetic Bearings Featuring Extremely Large Vertical Levitation Distances

Reto Bonetti, Dominik Bortis, Lars Beglinger and Johann W. Kolar  
 Power Electronic Systems Laboratory  
 ETH Zürich  
 Zürich, Switzerland  
 bonetti@lem.ee.ethz.ch

**Abstract**—This work provides an analytical method, based on the Ampèrian model of permanent magnets (PM), for a fast calculation of the magnetic flux density in three-dimensional space applying Biot-Savart law, and the calculation of the forces using Lorentz’s law. The applied approach enables the characterization regarding forces, torques, and stiffnesses of the levitating PM for any arbitrary position in space. Furthermore, it permits the extension of the investigation to any shape and configuration of ironless magnetic bearings (MB). In order to demonstrate the simple use of the analytical model, in this paper, the dimensions of an ironless axial MB employing PMs are optimized with a multi-objective Pareto analysis which reveals the physical limits concerning maximum achievable levitation height with respect to given constraints on, e.g., the required force and tilting stiffnesses, and the MB robustness defined by the maximum allowable payload on the levitating magnet. Moreover, the optimized axial MB and a corresponding test bench are realized to validate the proposed model with experimental results. For sake of completeness, it should be mentioned that in a later stage the optimized MB can also be scaled with simple scaling laws if the demanded specifications, e.g., concerning desired maximum levitation height or payload capability would have changed.

**Index Terms**—Magnetic levitation, Magnetic bearings, Permanent magnets, Biot-Savart law, Lorentz force, Multi-objective optimization

## I. INTRODUCTION

Magnetic bearings (MB) consisting of axially arranged permanent magnets (PM) and/or electromagnets (EM) are used, e.g., in suspension devices [1], in blood pumps [2], or in positioning applications where objects are levitated in vertical direction [3], and in certain cases even with extremely large levitation heights [4], [5] (see Fig. 1). Future applications could, e.g., be found in non-touch charging of drones and robotics, or even in manipulating objects inside a hermetically sealed process chamber. Such PM/EM arrangements have been analyzed in the literature [6]–[16], where, e.g., analytical equations for the resulting axial forces are derived. However, these closed-form equations are only valid for symmetric arrangements. Moreover, an investigation about the passive system stability, stiffness and robustness is not possible, since for these calculations, the forces and torques at a certain radial displacement have to be known. Therefore, time-consuming 3D FEM simulations have to be performed, where different possible MB geometries are iterated to obtain the optimal MB design.

As an alternative, in this paper, a simple analytical method based on the Biot-Savart law is proposed in Sec. II, which allows calculating the resulting forces and torques for any ironless non-symmetric 3D PM/EM geometry by substituting all PMs with equivalent current-carrying coils, so that the magnetic flux density distribution is replicated with sufficient accuracy. In contrast to [17], where the Ampèrian model is successfully applied to a simple linear Halbach array, the suggested method is not constrained by the shape of the PMs since the path of the Ampèrian model coils is discretized into short linear segments. Nonetheless, it is applied to an

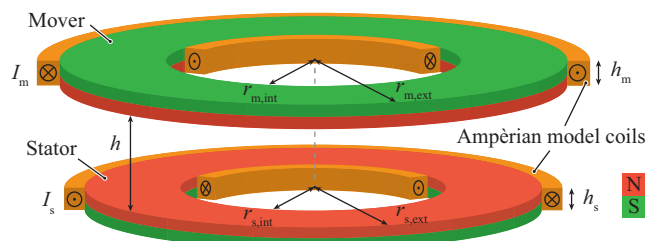


Fig. 1: General axial MB arrangement with ring-shaped PMs, where also the equivalent current-carrying coils are shown.

ironless axial magnetic bearing constituted by PMs with axial magnetization, as illustrated in Fig. 1. For instance, a similar arrangement with PMs and stator coils, which could also be analyzed with the proposed method, is found in motors featuring ironless coil units [18] where the back iron parts are explicitly omitted in order to eliminate attraction or cogging forces between PMs and iron cores, and to achieve superior positioning precision as well as fast dynamics with high acceleration and deceleration capabilities. Further applications are, e.g., found in weight optimized ironless flywheels where Halbach arrays are employed [19]. Moreover, the considered analytical model could also be used in combination with the method of images [20], to determine the magnetic forces and torques in MBs and motors incorporating PMs and simple structures of magnetic materials. In [21], for example, the method of images was applied in combination with the surface charge model of PMs [20] to calculate the radial and axial magnetic forces in an axial MB of a highly reliable fan, or in [22] it is used to design a suspension system for a micro-lithography application where precise movements are required.

In this paper, the purpose of using PMs in the axial MB is to generate large passive vertical forces, which result in an efficient levitation of the levitating PM, hereinafter called mover. However, as stated by Earnshaw’s theorem [23] (Sec. III), a passive stabilization of each degree of freedom (DOF) of the mover is not possible. Therefore, the proper integration of EMs is essential to actively control the remaining unstable DOFs of the mover and to stabilize its position. The design of the EMs is not further discussed in this work, however, in Sec. IV it is shown that the selected dimensions of the MB as well as the relative magnetization direction between the two PMs define which and how many DOFs remain unstable. Hence, different passive stability types depending on the number of passively stable DOF and stiffnesses are defined in Sec. IV.

To demonstrate the simple use of the analytical model, in Sec. V, the axial MB is optimized such that the maximum possible levitation height is achieved for given constraints as, e.g., the tilting stiffness and the maximum payload the mover can carry. As shown in Sec. VI, for a minimum tilting stiffness of  $1 \text{ mNm}/^\circ$  and a demanded payload capacity of 50 times the mover weight, the optimized axial MB features a maximum diameter of 130 mm, i.e., the characteristic dimension of the MB, a maximum magnet height of 21 mm, and a payload

capacity of 17 kg. Moreover, it is found that a characteristic dimension related levitation height (CDRLH) close to 1.0 can be achieved, clearly outperforming existing commercial systems, which achieve CDRLHs around 0.5 [4], where the levitation height is only half the characteristic dimension.

Further, in **Sec. VII**, the performance of the axial MB is tested on a 6DOF platform, where the stationary PM, hereinafter called stator, can be brought into different positions and distances relative to the mover in order to experimentally verify the analytically calculated forces and torques.

For the sake of completeness, instead of iterating through all possible combinations in the Pareto optimization, in **App. A**, scaling laws are derived from the analytical equations which directly allow calculating the resulting forces, torques, stiffnesses, and levitation height for a scaled version of the characterized MB.

## II. ANALYTICAL MODEL DESCRIPTION

### A. Ampèrian model of permanent magnets

As also described in [24] and applied in [15], [17], to replicate the magnetic field generated by the axially-magnetized ring PMs, current-carrying coils with the same inner and outer radius as well as the same height as the PMs can be used (see **Fig. 1**). The current direction is given by the polarity of the PMs, whereas the amplitudes  $I_s$  and  $I_m$  are determined with Ampère's law as [25]

$$I_i = \frac{H_{ci,i} \cdot h_i}{N_i} \quad \text{with } i = \{s, m\}, \quad (1)$$

where  $H_{ci,i}$  is the coercive field (955 kA/m for the investigated Neodymium-Iron-Boron magnets),  $h_i$  is the height of the PM, and  $N_i$  is the number of turns of the model coil.

In the following, for the approximation of the PM's magnetic flux density, a lumped single-turn coil ( $N_i = 1$ ) located at the center of the height  $h_i$  is assumed (see **Fig. 2** and **Fig. 4 (a)**). This choice, on the one hand leads to the lowest computation effort, while on the other hand for the far field calculation a sufficient accuracy is achieved. To also improve the accuracy of the near field calculation, a distributed multi-turn coil along the total height  $h_i$  is possible (**Fig. 4 (b)**), which consequently implies an increased computation effort.

### B. Simplified 2D analysis

To introduce the proposed analytical method, it is assumed that the internal radii  $r_{m,int}$  and  $r_{s,int}$  of the two ring-shaped PMs are zero. Hence, the most simple MB configuration with two disc-shaped PMs is obtained as depicted as cross-section view in **Fig. 2**.

For this axially symmetric arrangement, a simplified 2D analysis can be conducted, where each of the two PMs are substituted by two straight and infinitely long conductors carrying the same current  $I_{i1} = I_{i2}$  in opposite directions.

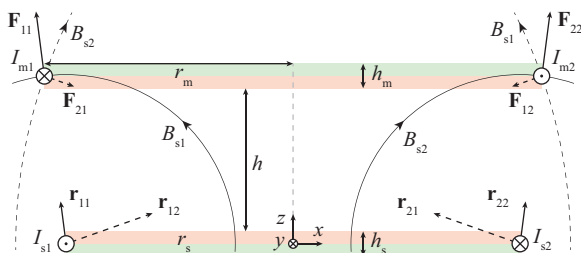


**Fig. 2:** Cross-section view of two disc-shaped PMs (see **Fig. 1** with  $r_{m,int} = r_{s,int} = 0$ ), explaining the Lorentz forces acting on the mover coils. Both conductors modeling the stator PM generate a force on both conductors modeling the mover PM, whose direction can be determined with the right-hand rule.

Based on Ampère's law, the magnetic flux density generated by each of the two stator conductors can be determined for each position in space, and decays with  $1/r$ , where  $r$  is the distance from the considered stator conductor to the magnetic flux density evaluation point. Based on the right-hand rule, the magnetic flux density, always points in tangential direction with respect to  $\mathbf{r}$  (see **Fig. 2**). Hence, the Lorentz force acting on each mover conductor can be directly determined with the superposition of the two force components acting from the two stator conductors. There, the force vector always lies in the connection line between the considered stator and mover conductors and, depending on the current directions, results in an attractive or repulsive force (see **Fig. 2**). Consequently, the total force acting on the mover is the sum of each force contribution, i.e.,  $\mathbf{F}_{tot} = \mathbf{F}_{11} + \mathbf{F}_{12} + \mathbf{F}_{21} + \mathbf{F}_{22}$ . For this symmetrical case, the total force only acts in the axial direction because the xy-forces cancel each other out. However, in the general case, where the mover is, e.g., displaced from the center in x-direction,  $\mathbf{F}_{tot}$  results in a net force component acting in x-direction. In addition, the z-force components acting on each of the two mover conductors are not equal, meaning that a torque in y-direction is created. Consequently, the mover experiences a horizontal displacement in x-direction while rotating around the y-axis. The 2D analysis of this general case, however, is only true for infinitely long and straight conductors, and can be applied to approximately calculate the forces for axially symmetric arrangements. Hence, to also investigate arbitrary configurations with, e.g., displaced or tilted movers, an analytic 3D analysis has to be performed.

### C. 3D analysis, magnetic flux density calculation

In a homogeneous medium, the Biot-Savart law allows calculating the magnetic flux density vector  $\mathbf{B}$  at any point in 3D space generated by a conductor carrying the current  $I_s$  as

$$\mathbf{B} = \frac{\mu}{4\pi} \int_C \frac{I_s d\mathbf{l}_s}{r^2} \times \frac{\mathbf{r}}{r}, \quad (2)$$

where in the following  $\mu = \mu_r \mu_0 = \mu_0$  is assumed. There,  $d\mathbf{l}_s$  is the vector representing an infinitesimally small piece of conductor pointing in the direction of the current  $I_s$ , and  $\mathbf{r}$  is again the distance vector between the considered piece of conductor and the evaluation point of the magnetic flux density. In case of a circular conductor, the solution of (2) contains elliptic integrals that need to be evaluated with numerical integration [26]–[28]. According to [29], the approach used in this paper is to approximate the integral of (2) with a finite sum of field components, such that the magnetic flux density generated by any kind of current-carrying conductor can be calculated. Accordingly, the single-turn coils of the mover and stator are discretized in a finite number  $N_{pts}$  of conductor segments with arc length  $\Delta l_i$ , which are represented by their corresponding center points as shown in **Fig. 3**.

Hence, in order to calculate the magnetic flux density at the center points of each mover segment, the magnetic flux density contribution of each stator segment has to be evaluated as

$$\Delta \mathbf{B}_j = \frac{\mu_0}{4\pi} \cdot \frac{I_s \Delta l_s}{r^2} \times \frac{\mathbf{r}}{r}, \quad (3)$$

where the length of the vector  $\Delta l_s$  is given by the arc length between two adjacent center points on the stator winding and its direction is determined by the direction of the current  $I_s$  at the corresponding center point, i.e., always tangential to the circular winding. The distance vector  $\mathbf{r}$  equals the distance between the considered center points.

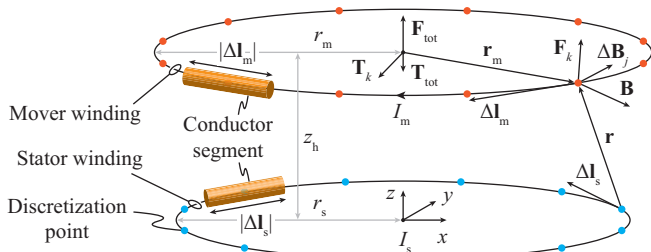


**Fig. 3:** Discretization of the Ampèrian model coils of **Fig. 1** for  $r_{m,int} = r_{s,int} = 0$  and  $N_s = N_m = 1$ , where the magnetic flux density, forces, and torques are reported.

Accordingly, the total magnetic flux density acting on one mover center point is given by

$$\mathbf{B} = \sum_{j=1}^{N_{pts}} \Delta \mathbf{B}_j = \frac{\mu_0}{4\pi} \sum_{j=1}^{N_{pts}} \frac{I_s \Delta \mathbf{l}_s}{r^2} \times \frac{\mathbf{r}}{r}. \quad (4)$$

### D. 3D analysis, force and torque calculation

Knowing the magnetic flux density at each mover coordinate or center point, the Lorentz force  $\mathbf{F}_k$  acting on each mover segment (**Fig. 3**) needs to be calculated to determine the total force applied the mover as

$$\mathbf{F}_{tot} = \int I_m d\mathbf{l}_m \times \mathbf{B} \approx \sum_{k=1}^{N_{pts}} \mathbf{F}_k = \sum_{k=1}^{N_{pts}} I_m \Delta \mathbf{l}_m \times \mathbf{B}. \quad (5)$$

Accordingly, the total torque referenced to the center of the mover winding is calculated by summing the radius-force products of each mover point, i.e.,

$$\mathbf{T}_{tot} = \sum_{k=1}^{N_{pts}} \mathbf{T}_k = \sum_{k=1}^{N_{pts}} \mathbf{r}_m \times \mathbf{F}_k, \quad (6)$$

where  $\mathbf{r}_m$  is the radius vector pointing from the center of the mover's winding to a segment center point on the mover winding.

The number of discretization points  $N_{pts}$  determines the precision of the finite sum approximation and the required computation time. It has been observed that for  $N_{pts} \gg 1$ , the force/torque error decays exponentially with  $N_{pts}$ , whereas the computation time grows quadratically with  $N_{pts}$ , since for the magnetic flux density calculation of each mover segment, each stator segment has to be considered. Consequently, for this work, a discretization of  $N_{pts} = 100$  was chosen, which reveals a sufficient accuracy at a moderate computation effort.

### E. Further considerations

In a case, where the stator and mover are realized as ring-shaped PMs, four model coils with radius  $r_{s,int}$ ,  $r_{s,ext}$ ,  $r_{m,int}$ , and  $r_{m,ext}$  are required, where the currents in the inner and outer coil of each ring-shaped PM are pointing in opposite direction (see **Fig. 1**). In the simplest case, where single-turn coils are considered (**Fig. 4 (a)**), the calculation of the forces and torques has to be conducted for all combinations of coil pairs, where a pair is constituted by a stator and a mover coil.

However, as already mentioned, the accuracy of the simulated magnetic flux density distribution depends on the coil's number of turns  $N_i$  and the distance  $h$  between the PMs (see **Fig. 4**). Especially in the near field region, a distributed multi-turn coil (**Fig. 4 (b)**) results in a more accurate field calculation compared to the lumped single-turn coil (**Fig. 4 (a)**). Hence, for relatively small distances  $h$  compared to  $h_i$  ( $h \ll h_s, h_m$ ), the multi-turn approach must be used. Thus, the

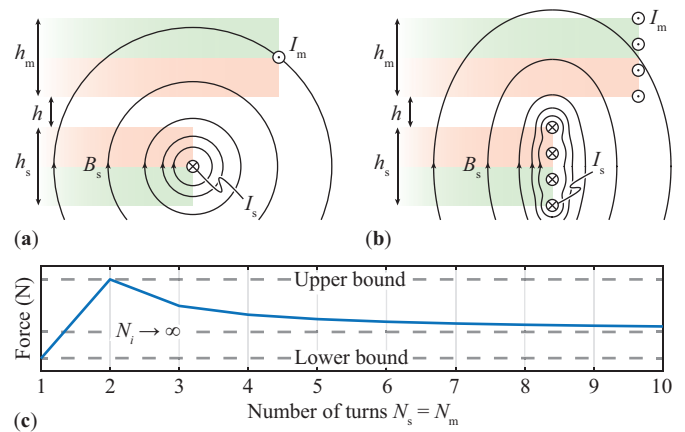


**Fig. 4:** Magnetic flux density distribution of the stator PM in a 2D plane for the case  $h \ll h_s, h_m$  with **(a)** single-turn model coils  $N_s = N_m = 1$  and **(b)** multi-turn model coils  $N_s = N_m = 4$ . **(c)** Example of force calculation for different numbers of model turns  $N_s$  and  $N_m$  considering the same MB, where it can be seen that the single and double-turn models define the bounds for all other force calculations with  $N_s = N_m \geq 3$ .

forces and torques between each stator and mover turn have to be calculated, which means that compared to the single-turn approach, the computational effort for the multi-turn winding approach increases by  $N_s \cdot N_m$ .

For the considered axial MB, however, where extremely large levitation heights are pursued, i.e.,  $h \gg h_s, h_m$ , the single and the multi-turn models result in a similar far field distribution; thus, similar forces and torques are obtained as shown later in **Fig. 6**, **Fig. 15** and **Sec. VI**. This justifies the described procedure, where in a first step, the single-turn coil approach is used for a coarse Pareto optimization to speed up the computation time, while in a second step, the force and torque calculation is refined to obtain precise results (see **Fig. 15 (b)-(d)**).

Furthermore, there is an interesting fact that the single-turn ( $N_s = N_m = 1$ ) and the double-turn model ( $N_s = N_m = 2$ ) define the bounds for the calculated forces and torques, whereas the multi-turn models with  $N_s = N_m \geq 3$  yield values between these bounds, i.e., the calculation error decays with increasing number of model turns as it is shown in **Fig. 4 (c)** for a particular case with randomly selected values for  $h$ ,  $h_s$ , and  $h_m$  and as also verified later for the force calculations of the optimal MB (see **Fig. 15**).

## III. PASSIVE STABILITY

The derived analytical method enables an extensive analysis regarding the behavior of the mover in 3D space. Therefore, in a first step of the design process, the passive stability of the mover, i.e., the DOFs which are already passively stable only due to the presence of the PMs, is analyzed for its nominal operating or levitation position. As stated by Earnshaw's theorem [23], not all six DOFs of the mover (see **Fig. 5 (a)**) can be stabilized passively. However, as shown in the following, depending on the selected dimensions of the axial MB, different stability types with different amount of passively stable DOFs or different properties concerning stiffnesses are obtained. At the end, a stability type which on the one hand enables a high levitation height, and on the other hand minimizes the sensing and control effort of the EMs to actively control the remaining unstable DOFs, should be selected.

### A. Displacement Method

The applied method to determine the passively stable DOFs of the mover is to displace the mover from a nominal levitation

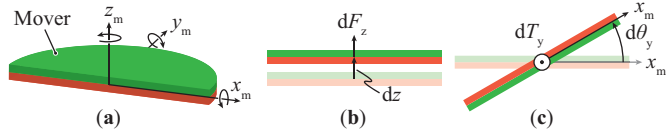


**Fig. 5:** (a) Illustration of the mover's six DOF with its coordinate system spanned by  $(x_m, y_m, z_m)$ , where a translation and a rotation along each axis is possible. (b) Axial displacement of the mover needed to calculate the gradient  $dF_z/dz$ . (c) Rotation around the  $y$ -axis of the mover needed to calculate the gradient  $dT_y/d\theta_y$ .

position, e.g., vertically centered above the stator, and to compute all forces and torque for this position. From these values, for each DOF, the corresponding force and torque gradients can be determined, e.g., the axial force gradient  $dF_z/dz$  is determined by calculating the change of force  $dF_z$  for a certain displacement  $dz$  of the mover in  $z$ -direction (**Fig. 5 (b)**). Similarly, to calculate the torque gradient of a rotational DOF, the mover is tilted or rotated as, e.g., illustrated in **Fig. 5 (c)** to obtain the torque gradient  $dT_y/d\theta_y$ . As a result, a negative gradient value, i.e., a force or torque acting in opposite direction to the virtual displacement, is associated with a stable equilibrium, whereas a positive gradient value indicates an unstable equilibrium. The magnitude of the gradient is defined as stiffness, which characterizes the dynamic behavior of the mover around the equilibrium. A gradient that equals zero means that the equilibrium is marginally stable, i.e., neither stable nor unstable.

### B. Passive stability types

These force and torque gradients as well as the stiffnesses are now analyzed for the axial MB. If the mover is located at its nominal axially centered position at a certain height  $h$  (the MB is axially symmetric) the following holds

$$F_x = F_y = 0 \quad (7) \quad dF_x/dx = dF_y/dy \quad (10)$$

$$T_x = T_y = 0 \quad (8) \quad dT_x/d\theta_x = dT_y/d\theta_y \quad (11)$$

$$T_z = 0 \quad (9) \quad dT_z/d\theta_z = 0. \quad (12)$$

In contrast to the general case, (10), (11), and (12) imply that the stability properties for the axially symmetric MB can be derived with a reduced computation time, since only three gradients have to be determined, i.e.,  $dF_x/dx$ ,  $dF_z/dz$ , and  $dT_y/d\theta_y$ . Another direct implication of (12) is the marginal stability of the torque in axial direction. Moreover, as explained in [23] and applied in [1], [6], [7], [21], the divergence of the force vector between permanent magnets in a homogeneous medium is given as

$$\nabla \cdot \mathbf{F} = \frac{dF_x}{dx} + \frac{dF_y}{dy} + \frac{dF_z}{dz} = 0, \quad (13)$$

which in combination with (10) results in

$$\frac{dF_z}{dz} = -2 \cdot \frac{dF_x}{dx}. \quad (14)$$

It is important to mention that even though (14) holds for the arrangement presented in this paper, the proposed analytical model does not rely on these assumptions regarding symmetry, however, they have been observed as a result of the calculations. Consequently, the following conclusions can be drawn. First, (14) excludes a simultaneous stability of all three force components. Second, a passive force stability is only possible in either axial or radial direction, and third, at least one force component must be stable, thus a passive stability type with only torque stability is not possible. Consequently, with these restrictions given for axially symmetric MBs with

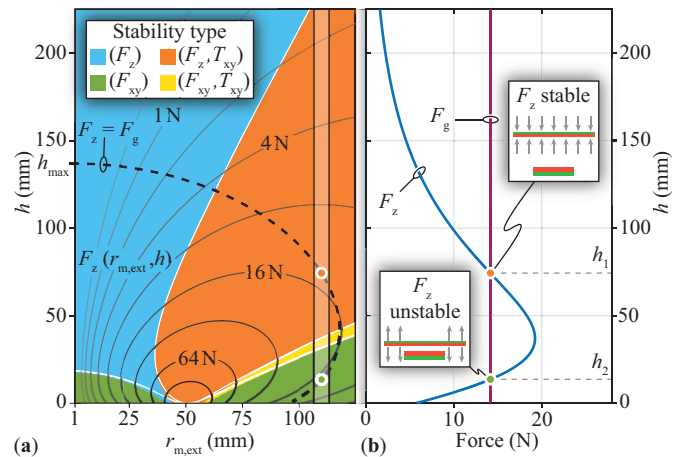


**Fig. 6:** (a) Stability regions for different levitation heights  $h$  depending on the mover radius  $r_{m,ext}$  for two axially centered disc-shaped PMs with  $r_{s,ext} = 50$  mm,  $h_m = 5$  mm, and  $h_s = 10$  mm. (b) Axial magnetic force versus axial position of the mover with  $r_{m,ext} = 110$  mm, where the levitation positions for  $F_z = F_g$  are highlighted. The gradient of  $F_z$  reveals that at  $h_1$  the passive levitation is stable, while at  $h_2$  it is unstable.

both magnets centered on the axial axis, only four types of passive stability are possible:

- I.  $(F_z)$ : the mover is stable against axial displacements, i.e., only one DOF is passively stable;
- II.  $(F_{xy})$ : the mover is stable against radial displacements, i.e., two DOFs are passively stable;
- III.  $(F_z, T_{xy})$ : in addition to  $(F_z)$ , the mover is also stable against tiltings in  $xy$ -direction, i.e., three DOFs are passively stable;
- IV.  $(F_{xy}, T_{xy})$ : in addition to  $(F_{xy})$ , the mover is also stable against tiltings in  $xy$ -direction, i.e., four DOFs are passively stable.

The advantage of the stability types  $(F_{xy}, T_{xy})$  and  $(F_z, T_{xy})$  over the other stability types is the lower number of unstable DOFs, which translates to a simpler design of the active controller. Since  $T_z$  is marginally stable and for the axial MB must not be actively stabilized, with  $(F_z, T_{xy})$  only two DOFs, i.e., the radial displacement in  $xy$ -direction, and with  $(F_{xy}, T_{xy})$  only one DOF, i.e., the levitation height in  $z$ -direction, have to be actively controlled.

### IV. DEPENDENCE OF MB DIMENSIONS ON LEVITATING PROPERTIES

The question now arises how the axial MB has to be designed such that a certain stability type with a high stiffness is obtained. In order to demonstrate this, this section starts with a design example consisting of two disc-shaped PMs with opposing magnetization direction. There, the mover's external radius  $r_{m,ext}$  is used as a variable, whereas the other dimensions are chosen as  $r_{s,ext} = 50$  mm,  $r_{s,int} = r_{m,int} = 0$  mm,  $h_s = 10$  mm, and  $h_m = 5$  mm. In the following, it is shown that with different  $r_{m,ext}$ , different stability types are obtained. Furthermore, it is highlighted that the passive tilting stiffness of the mover can be improved by using ring-shaped instead of disc-shaped PMs.

#### A. Stability regions and levitation height

The first step of the design example is to determine the stability type obtained for different  $r_{m,ext}$  and levitation heights  $h$  combinations, while the radial position is always kept zero.

**Fig. 6 (a)** shows the resulting stability types derived with the displacement method for each  $r_{m,ext}$ - $h$  combination. It can be noticed that the preferred stability types with the highest number of passively stable DOFs, i.e.,  $(F_z, T_{xy})$  in the

orange region and  $(F_{xy}, T_{xy})$  in the yellow region, are only obtained for  $r_{m,ext} \geq 36$  mm. It should be mentioned that the colored regions have been generated with the fast model ( $N_s = N_m = 1$ ), and the boundaries between the regions have been proven to be satisfyingly precise with the multi-turn model  $N_s = N_m = 4$  as indicated with white lines.

To complete the picture, the levitation height  $h$  at which the mover will passively settle has to be determined, which is found for the case where the axial force  $F_z$  is equal to the gravitational force  $F_g$  of the examined PM, i.e.  $F_z = F_g$ , as indicated in **Fig. 6 (a)** with a dashed line. It can be noted that with the smallest considered mover radius  $r_{m,ext}$  the largest levitation height of  $h_{max} = 137$  mm is achieved. At this design point, however, only  $F_z$  is passively stable, meaning that tiltings and radial displacements of the mover have to be actively controlled. Furthermore, only low axial forces  $F_z$  and low MB stiffnesses are achieved. Therefore, it is beneficial to choose a design point in the orange region  $(F_z, T_{xy})$ , where at the expense of a certain levitation height reduction (min. 2.5%), a passive tilting stability in xy-direction is gained, such that only the mover's radial displacements in xy-direction have to be actively controlled.

With a further increase of  $r_{m,ext}$ , the levitation height  $h$  continuously decreases and above a certain value even two operating points with  $F_z = F_g$  are found. To explain this behavior, **Fig. 6 (b)** illustrates the calculated axial magnetic force  $F_z$  with respect to  $h$  for  $r_{m,ext} = 110$  mm. As can be noted, only the levitation height  $h_1$  is passively stable, since at lower  $h < h_1$ , the axial force increases ( $F_z > F_g$ ) and therefore would lift the mover up again. This is also found by the fact that the force gradient  $dF_z/dz$  around this operating point is negative (stable), while around  $h_2$  it is positive (unstable).

Hence, with the above considerations, for the design example the mover radius is chosen to be  $r_{m,ext} = 63$  mm which means that the levitation height is maximized for the stability type  $(F_z, T_{xy})$  (see **Fig. 6 (a)**). For the sake of completeness, it should be mentioned that the yellow region with stability type  $(F_{xy}, T_{xy})$ , which offers the highest number of passively

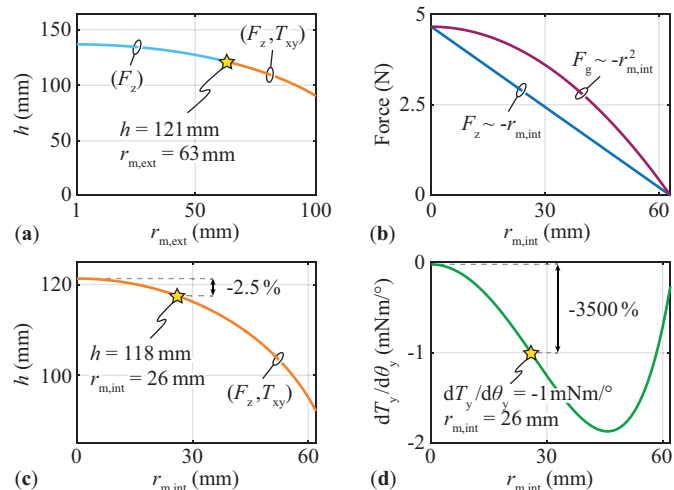


**Fig. 7:** MB design example starting from two disc-shaped PMs with fixed dimensions  $r_{s,ext} = 50$  mm,  $r_{s,int} = 0$  mm,  $h_s = 10$  mm, and  $h_m = 5$  mm. (a) Levitation height versus mover external radius with  $r_{m,int} = 0$  mm (see dashed line in **Fig. 6 (a)**). With the optimal radius  $r_{m,ext} = 63$  mm, the largest levitation height for the stability type  $(F_z, T_{xy})$  is obtained. Trends of (b) the axial and gravitational forces, (c) the levitation height  $h$ , and (d) the tilting stiffness with respect to the mover internal radius  $r_{m,int}$ .  $r_{m,int}$  is selected to be 26 mm such that a tilting stiffness of 1 mNm/° is ensured, while the reduction in levitation height  $h$  is small.

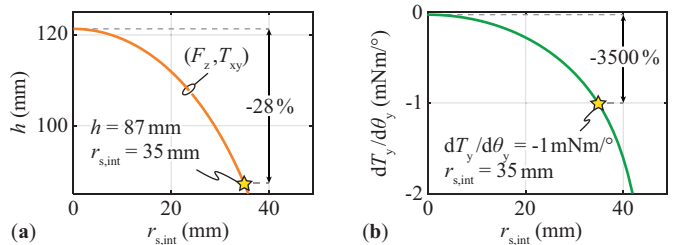


**Fig. 8:** MB design example starting from two disc-shaped PMs with fixed dimensions  $r_{s,ext} = 50$  mm,  $h_s = 10$  mm,  $h_m = 5$  mm,  $r_{m,int} = 0$  mm, and  $r_{m,ext} = 63$  mm. (a) Resulting levitation height  $h$  and (b) tilting stiffness depending on the internal stator radius  $r_{s,int}$ . To achieve a tilting stiffness of 1 mNm/° by varying  $r_{s,int}$ , a much stronger reduction in levitation height  $h$  has to be accepted compared to the case where  $r_{m,int}$  is varied.

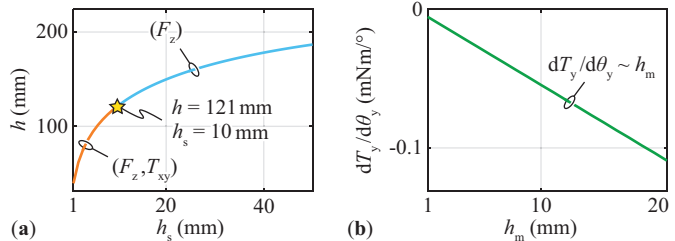


**Fig. 9:** MB design example starting from two disc-shaped PMs with fixed dimensions  $r_{s,ext} = 50$  mm,  $r_{s,int} = r_{m,int} = 0$  mm, and  $r_{m,ext} = 63$  mm. (a) Levitation height  $h$  with respect to the stator height  $h_s$ , where the mover height is fixed to  $h_m = 5$  mm. An improvement of the levitation height for increasing  $h_s$  is observed, but is limited by the stability type region. (b) Linear trend of the tilting stiffness versus mover height  $h_m$ , where the stator height is  $h_s = 10$  mm.

stable DOFs, is relatively narrow; thus, is difficult to obtain, and also results in an much lower levitation height compared to  $(F_z, T_{xy})$ .

### B. From disc-shaped to ring-shaped PMs

A further possibility to increase the levitation height  $h$  is, e.g., to reduce the mover weight and, therefore, the gravitational force  $F_g$  by increasing its internal radius  $r_{m,int}$ , i.e., by passing from a disc-shaped to a ring-shaped mover PM. At the same time, however, also a decrease of the axial force  $F_z$  has to be expected, since the needed additional model coil placed at the mover's internal radius (**Fig. 1**) generates an attractive force in combination with the stator coil due to its opposite current direction compared to the external mover coil. As derived in **App. A** and shown in **Fig. 7 (b)**, even though  $F_g$  reduces with the square of  $r_{m,int}$ , while the axial force  $F_z$  only decays proportionally with  $r_{m,int}$ , the levitation height  $h$  decreases with increasing  $r_{m,int}$  (see **Fig. 7 (c)**), since  $F_z$  is always lower than  $F_g$  as highlighted in **Fig. 7 (b)**. However, as illustrated in **Fig. 7 (d)**, the major advantage of a ring-shaped mover compared to a disc-shaped magnet ( $r_{m,int} = 0$  mm) is the fact that with increasing  $r_{m,int}$  (up to  $r_{m,int} = 46$  mm), the negative torque gradient and thus also the tilting stiffness (magnitude of the gradient) are substantially increasing. Assuming a minimum required tilting stiffness of 1 mNm/°, an optimum internal mover radius of  $r_{m,int} = 26$  mm is found. This 35 times larger stiffness compared to the disc-shaped mover PM comes at the expenses of only 3 mm in levitation height, i.e., a reduction of 2.5% (cf. **Fig. 7 (a)** and (c)).

The same sensitivity analysis can also be conducted for the stator internal radius  $r_{s,int}$ , while again a disc-shaped mover with  $r_{m,ext} = 63$  mm is assumed. For the ring-shaped stator, an additional model coil with opposite current direction has to be considered, which results in a reduction of the axial force

$F_z$ . Since the mover's dimensions are kept constant, also  $F_g$  of the mover remains constant. Consequently, the levitation height decreases with increasing  $r_{s,int}$  as shown in **Fig. 8 (a)**. As already observed for the variation of  $r_{m,int}$ , the tilting stiffness increases for a ring-shaped stator (see **Fig. 8 (b)**), however, to reach the same stiffness as with a ring-shaped mover, the levitation height drops substantially by 34 mm, i.e., 28 % compared to a disc-shaped stator.

Besides changing the inner and outer radii of the PMs, also the PM heights  $h_s$  and  $h_m$  can be varied. Starting with the variation of the stator height  $h_s$ , while keeping the other PM dimensions constant ( $r_{s,ext} = 50$  mm,  $r_{s,int} = r_{m,int} = 0$  mm,  $r_{m,ext} = 63$  mm, and  $h_m = 5$  mm), it is expected (and also mathematically derived in **App. A**) that the axial force increases linearly with  $h_s$ , since based on (1) also the equivalent coil current, and thus the Lorentz force increase linearly. This means that the levitation height  $h$  increases, as the gravitational force of the mover remains unchanged. However, as already observed in **Fig. 6**, the stability type changes depending on the levitating height  $h$ . Consequently, for the design example, the stator height must be limited below  $h_s = 10$  mm, to maintain the desired stability type  $(F_z, T_{xy})$  (see **Fig. 9 (a)**).

Now, for the fixed stator height  $h_s = 10$  mm, the mover height  $h_m$  is varied to address the corresponding stiffness sensitivity. As detailed in **App. A**, all forces and gradients scale linearly with  $h_m$ , which means that also the tilting stiffness increases (see **Fig. 9 (b)**). However, the levitation coordinate  $z_h$  (the axial coordinate of the mover's center point) remains the same, while the effective levitation height  $h$  decreases with increasing mover height ( $h = z_h - h_s/2 - h_m/2$ ). Thus,  $h_m$  can finally be used to tune the stability properties, while again a slight levitation height reduction has to be accepted.

Concluding this section, the simple example showed that the effective levitation height  $h$  cannot be increased by reducing the weight of the mover, i.e., increasing the internal radius  $r_{m,int}$ . However, with a ring-shaped mover, a strongly enhanced tilting stiffness can be gained at the expense of a slight levitation height reduction. Similarly, with a ring-shaped stator, the tilting stiffness can also be increased, but the reduction in levitation height is much stronger. In contrast, the stator height  $h_s$  increases the levitation height only up to some extent, determined by the stability type of the levitation point. Finally, by varying the mover height  $h_m$ , the stiffnesses can be linearly tuned, affecting the levitation height by  $-h_m/2$ .

## V. OPTIMIZATION PROCESS

In the example above, only one dimension has been varied at a time to analyze the sensitivity of the levitation height  $h$  on different design parameter and to determine the passive stability properties. In the following, an optimization is performed where all mentioned dimensions are varied iteratively and the resulting characteristics of the levitation points are determined to find the optimal axial MB arrangement for the given application requirements.

### A. Optimization targets

In the design process, for a given geometry, the resulting levitation height  $h$  is determined, where the mover is assumed to be centered on the axial axis and  $F_z = F_g$  (see  $LP_1$  and  $LP_2$  in **Fig. 10 (a)**). Afterwards, the gradients of three mover's DOF, i.e.,  $dF_x/dx$ ,  $dF_z/dz$ , and  $dT_y/d\theta_y$  of these levitation heights are calculated, such that the stiffnesses and the stability properties can be obtained. Due to the axial symmetry of the MB, also the remaining gradients can be evaluated with (10)-(12). From the obtained passive stabilities, the stability types can be determined. For the optimization process, only

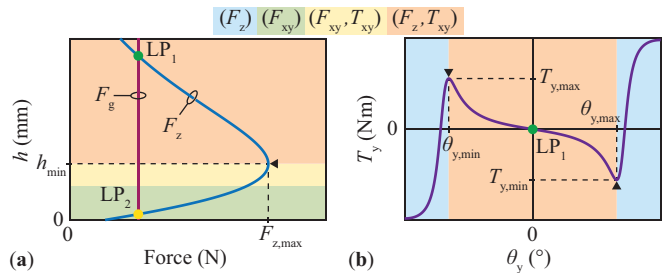


**Fig. 10: (a)** Illustration of the axial robustness with passively stable levitation point  $LP_1$ . The mover can be loaded with an additional payload up to  $F_{z,max}$  before the stability properties of the original levitation point are violated. **(b)** Illustration of the rotational robustness for the levitation point  $LP_1$  of **(a)**. As soon as the maximum torque/rotation  $T_{y,max}$  is exceeded, the mover loses its ability to reject external torque disturbances.

designs with  $(F_z, T_{xy})$  and  $(F_{xy}, T_{xy})$ -stability are considered ( $LP_1$  in **Fig. 10 (a)**), whereas designs with other stabilities are discarded ( $LP_2$  in **Fig. 10 (a)**).

A further essential aspect is the achievable robustness, which is a measure for the magnitude of the external disturbance or the maximum displacement/rotation the mover can withstand maintaining the same stability properties as in the original levitation point, and can be divided into three categories.

The *axial* robustness is defined as the maximum axial force  $F_{z,max}$  that can be applied to the mover, i.e., the maximum payload capacity (**Fig. 10 (a)**). This means that, e.g., the mover levitating at  $LP_1$  can be loaded with an additional payload. Consequently, the levitation height reduces, until for the maximum payload, the minimum levitation height  $h_{min}$  is achieved. For levitation height below  $h_{min}$ , the stability properties change, meaning that the active control has to be changed and the payload has to be reduced again.

The *rotational* robustness is defined as the maximum torque the mover can withstand such that the same stability type as in the horizontal position can be maintained (**Fig. 10 (b)**). Rotations with an angle larger than  $\theta_{y,max}$  cause the mover to lose its ability to stabilize tilting disturbances. The shown torque curve versus the tilting angle is an odd function since the mover is centered on the axial axis; therefore, it holds  $\theta_{y,min} = -\theta_{y,max}$  and  $T_{y,min} = -T_{y,max}$ .

The *radial* robustness is related to the maximum deviation/displacement of the mover from the axial center position in x-direction  $x_{max}$  until the mover loses its initial stability properties obtained at the levitation point with  $x = 0$  (**Fig. 11**). The initial levitating position is indicated with  $LP_1$ , where the mover levitates horizontally centered on the axial axis.

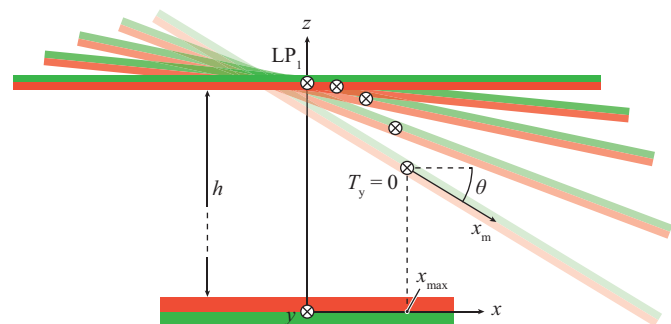


**Fig. 11: Cross-section view of the PMs with the mover initially positioned at the levitation point  $LP_1$  of **Fig. 10 (a)** and subjected to a radial displacement in x-direction to determine the radial robustness. For each x-position, the tilting angle  $\theta$  has to be determined such that  $T_y = 0$ . For  $x > x_{max}$ , the mover loses a stable component of the initial stability type  $(F_z, T_{xy})$ .**

For each investigated x-position ( $x > 0$ ), the new force and torque equilibrium has to be found, in which the mover has only to be actively stabilized in axial or radial direction, depending on the stability type at LP<sub>1</sub>. This is done in two steps: the tilt angle  $\theta$  has to be determined such that the y-torque becomes zero ( $T_y = 0$ ), while the new levitation height is again found with  $F_z = F_g$ . Hence, compared to the axial and rotational robustness, the computational effort is larger due to the iterative computation to find the equilibrium position for each x-position. It should be mentioned that for  $(F_z, T_{xy})$  stable MBs, it is important to have a wide range of radial robustness since this also allows the mover to deviate from its nominal axially centered position, and gives the sensor and the position controller enough headroom to sense a position change and bring the mover back to its nominal levitation position again. In contrast, for  $(F_{xy}, T_{xy})$  stable MBs,  $x_{max}$  is related to the passive robustness since in this case, the radial position is not actively controlled.

### B. Multi-objective optimization

As mentioned, the proposed geometry optimization is conducted by varying the dimensions of the MB and calculating their levitation points, stability properties, and robustnesses. Moreover, an additional degree of freedom is given by the relative magnetization direction between stator and mover. For two disc-shaped PMs, a repulsive force is only obtained for PMs having opposite polarities. However, when at least one PM is realized as a ring-shaped PM, depending on the dimensions, both relative magnetization directions can result in a repelling force. Therefore, in the optimization process seven design parameters could be iterated:  $r_{s,int}$ ,  $r_{s,ext}$ ,  $h_s$ ,  $r_{m,int}$ ,  $r_{m,ext}$ ,  $h_m$ , and the relative magnetization direction. In order to reduce the computation effort, in the following, the stator external radius is fixed to  $r_{s,ext} = 50$  mm. As shown in **App. A**, based on the derived scaling laws, the resulting optimum MB can be scaled to any other external stator radius in a post-processing step. Due to the same reason, also the mover height is fixed to  $h_m = 5$  mm, since in a post-processing step, the forces and torques can be scaled linearly with the mover magnet thickness  $h_m$  (see **App. A**). Hence, the optimization is constrained to the remaining five design parameters:  $r_{s,int}$ ,  $h_s$ ,  $r_{m,int}$ ,  $r_{m,ext}$ , and the relative magnetization direction.

## VI. OPTIMIZATION RESULTS

In **Fig. 12 (a)**, the optimization results of all geometries, which result in a  $(F_z, T_{xy})$  stability type, are represented as a 3D Pareto plot, where the maximum levitation height related to the characteristic dimension of each design, i.e., the *characteristic dimension related levitation height* (CDRLH), is evaluated with respect to its *axial relative payload capability*  $F_{z,max}/F_g$  and its *rotational absolute tilting stiffness*  $dT_y/d\theta_y$ . In addition, the color bar highlights the *gradient of the unstable xy-force component*  $dF_x/dx$  (due to symmetry reasons same as  $dF_y/dy$ ), which can be related to the required magnetomotive force (MMF) generated by the EMs, i.e., the amount of current fed to the EMs to actively control the mover position. It should be mentioned that the remaining *radial* robustness is not considered in the Pareto plot; thus, is only calculated for a set of optimal design candidates in a post-processing stage.

As expected, a larger CDRLH results in lower payload capability and xy-stiffnesses, since with increasing CDRLH, the magnetic flux density strength and consequently the forces decrease. As can be noted, a maximum CDRLH around 1.5 would be possible, however, in these cases, the axial and

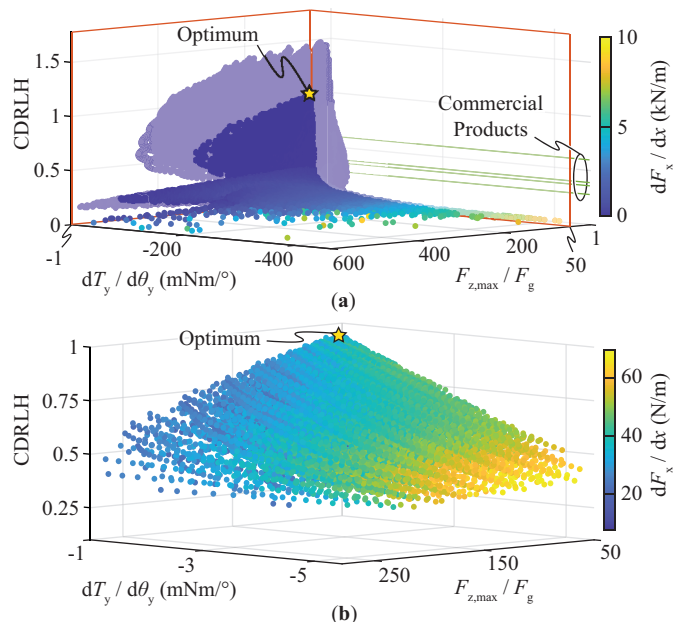


**Fig. 12:** Pareto plot of (a) all geometries, which result in a  $(F_z, T_{xy})$  stability type and (b) remaining designs with minimum relative payload capacity of  $F_{z,max}/F_g = 50$  and minimum absolute tilting stiffness  $dT_y/d\theta_y = -1$  mNm/°. The color bar corresponds to the gradient of the unstable xy-force component  $dF_x/dx$ , which has to be compensated by the magnetomotive force (MMF) of the EMs.

**TABLE I:** Optimal MB dimensions highlighted in **Fig. 12**.

Mover	Value	Stator	Value
$r_{m,ext}$	65 mm	$r_{s,ext}$	50 mm
$r_{m,int}$	36 mm	$r_{s,int}$	28 mm
$h_m$	5 mm	$h_s$	21 mm
Mag. Direction	Down	Mag. Direction	Up

rotational robustnesses tend to zero, which is not acceptable for a real MB design. Therefore, the optimization results are restricted to a range with a minimum relative payload capability  $F_{z,max}/F_g = 50$  and a minimum absolute tilting stiffness  $dT_y/d\theta_y = -1$  mNm/°. The Pareto plot of the remaining design points is shown in **Fig. 12 (b)**. There, also designs with very large gradients  $dF_x/dx$  with respect the unstable xy-force component are discarded (N/m instead of kN/m), since for the subsequent EM design a low MMF is desired. With these constraints, still a high CDRLH of around 0.95 can be achieved, which is clearly outperforming existing commercial products with CDRLH of around 0.6 [4], especially in the sense that at the same time a ten times higher payload capability is obtained.

In **Tab. I**, the mover and stator dimensions of the optimal design highlighted in **Fig. 12** are listed. The corresponding performance characteristics are given in **Tab. II**, where for

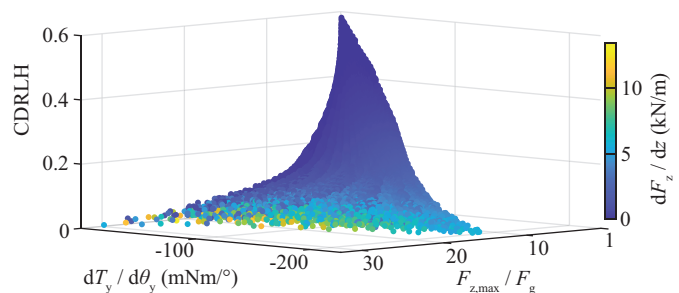


**Fig. 13:** Pareto plot of all geometries, which result in a  $(F_{xy}, T_{xy})$  stability type. Advantageously, only one DOF would have to be controlled, however, the achievable CDRLH and especially the payload capacity are much lower compared to the  $(F_z, T_{xy})$  stability type.

**TABLE II:** Calculated performance characteristics of the optimal geometry highlighted in Fig. 12 for single or multi-turn model coils.

Parameter	$N_s = N_m = 1$	$N_s = N_m = 10$
$h$	123.2 mm	123.8 mm
CDRLH	0.948	0.952
$dF_x/dx$	33.6 N/m	33.7 N/m
$dF_z/dz$	-65.8 N/m	-66.0 N/m
$dT_y/d\theta_y$	-1 mNm/°	-1 mNm/°
$T_{y,max}$	13.4 mNm	13.7 mNm
$\theta_{y,max}$	18°	18°
$x_{max}$	16 mm	16 mm
$F_{z,max}/F_g$	55.8	50.7
Mover Mass $m_m$	0.35 kg	0.35 kg
Payload Cap.	19.1 kg	17.4 kg

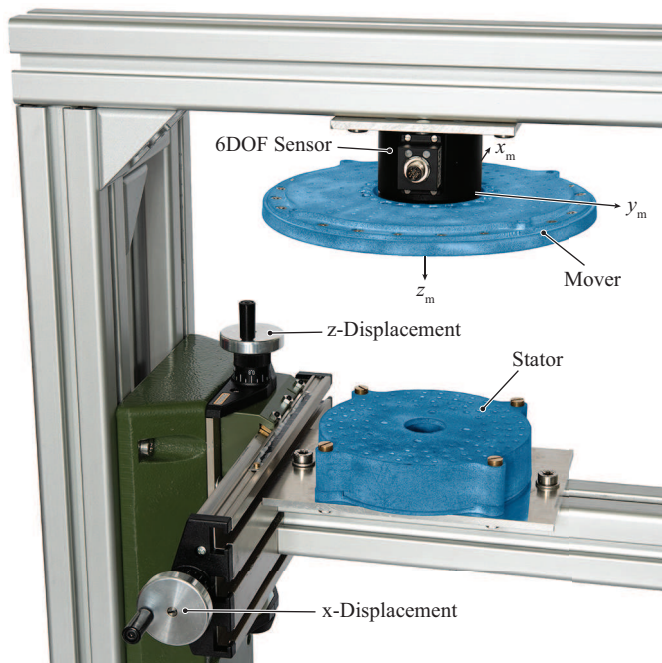


**Fig. 14:** Test setup showing the essential components, where the stator can be precisely moved against the fixed mover in x and z-direction with a positioning stage. The mover is mounted to a 6DOF sensor (Rokubi of BOTA Systems) which records all forces and torques applied to the mover with a resolution of 0.15 N and 5 mNm, respectively. Stator and mover are realized with a 3D-printed housing where a large number of small PMs (quality N45) are inserted.

the single and multi-turn coil approach similar results are obtained. As can be noticed, the optimum external mover radius  $r_{m,ext}$  is larger than the stator radius  $r_{s,ext}$ , thus defines the characteristic dimension to  $2 \cdot r_{m,ext} = 130$  mm. The absolute levitation height  $h$  is around 120 mm, while the mover can be tilted up to 18°, while a maximum radial displacement of 16 mm is allowed until the mover becomes unstable. Furthermore, the maximum payload  $F_{z,max}$  which can be carried by the mover is almost 20 kg, resulting in a strongly reduced passive levitation height.

For the sake of completeness, the same Pareto optimization was also performed for all geometries which result in a  $(F_{xy}, T_{xy})$  stability type, since in this case only the z-position would have to be controlled actively. However, as shown in Fig. 13, lower CDRLHs (max. 0.6) and especially much lower payload capacities (even below the lower limit used for the  $(F_z, T_{xy})$  stability type) are obtained.

## VII. EXPERIMENTAL VERIFICATION

In order to validate the analytic model, a test setup to measure the forces and torques acting on the mover is built as

illustrated in Fig. 14. In contrast to the final MB setup, where the mover is freely levitating above the fixed stator, in the test setup, the stator can be precisely moved against the fixed mover in x- and z-direction by means of a positioning stage. There, the mover is mounted to a 6DOF sensor which records all forces and torques applied to the mover.

In the test setup, both PMs are realized with a large number of small rectangular PMs, which are stacked together in a 3D-printed housing having the same dimensions listed in Tab. I. Hence, due to the free space between the individual rectangular PMs, the magnetic volume of the stator and mover PM is reduced (see Fig. 15 (a)), meaning that lower effective forces and torques are obtained. The PM volume reduction can be thought of as a proportional reduction of magnetic dipoles in a given mover/stator volume, thus, based on Ampère's law given in (1), this results in an equivalent reduction of the stator's and mover's coercive field strength  $H_{ci,s}$  and  $H_{ci,m}$  if a constant mover/stator volume is assumed. The reduction factors are determined from the volume ratio of the discrete PMs and the originally calculated ring-shaped PM volume, which for the built stator and mover leads to 78% and 74%, respectively. The magnetic force scales with  $H_{ci,s} \cdot H_{ci,m}$  and, therefore, reduces to 58% with respect to the optimal ring-shaped PMs. However, since the gravitational force of the mover does not scale with the same factor as the magnetic force - it scales proportionally with the mover PM volume - the scaling laws derived in App. A cannot be applied, which means that the new MB characteristics have to be recalculated by using the reduced  $H_{ci,s}$  and  $H_{ci,m}$  in the analytical model.

The corresponding calculated and measured axial forces for a radially centered mover position, i.e.,  $x = y = 0$ , with respect to the distance  $h$  are shown in Fig. 15 (c). As can be noted, the axial force monotonically increases with reduced

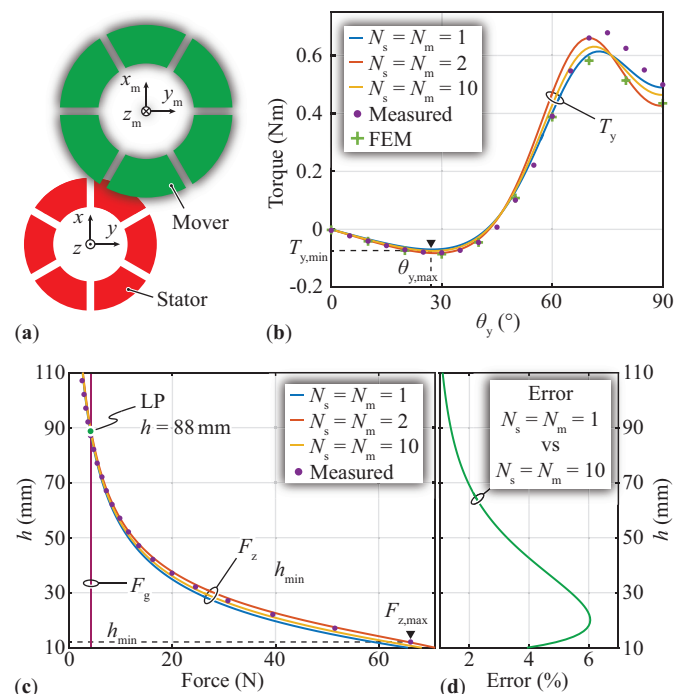


**Fig. 15:** (a) Top view of the schematic realization of the PMs of Fig. 14, where discrete magnets instead of ring-shaped PMs are utilized. (b) Comparison of the calculated and measured torque for a tilted but radially centered mover at the levitation height  $h = 88$  mm, where the tilting stiffness and the rotational robustness can be verified. (c) Comparison of the calculated and measured axial force for a radially centered mover which is only axially displaced; thus, the levitation point (LP) and the maximum payload capacity can be determined. (d) Calculation error between single and multi-turn model.

height  $h$ , which means that depending on the additional payload, all levitation heights are at least ( $F_z$ ) stable. The axial force derived with the multi-turn model lies always in between the forces calculated with the single and double-turn model; for the given setup, even at low distances  $h$ , the calculation error is below 6% as shown in **Fig. 15 (d)**. Furthermore, all models provide a good correspondence with the performed measurements.

Even though the mover is not actively levitated in the test setup yet, the levitation point can be found by comparing the axial force with the mover's gravitational force and would result in  $h = 88$  mm. In addition, the axial force stiffness at the levitation point is obtained from the force gradient  $dF_z/dz = -94$  N/m, which based on (14) directly gives the radial stiffness of  $dF_x/dx = 47$  N/m. The axial force measurement also permits to determine the maximum payload capacity of 6.3 kg at the minimum achievable levitation height of  $h = 12$  mm, which is limited by the 3D-printed housing thicknesses of the stator and mover ( $h$  is intended as the distance between the PMs' surfaces to be consistent with the definition used in this paper).

At the levitation point  $h = 88$  mm, the realized MB with radially centered mover is also characterized with respect to its rotational stiffness, where the torque  $T_y$  is calculated and measured for different tilting angles  $\theta_y$  as depicted in **Fig. 15 (b)**. Again, the results obtained with the single and multi-turn models are in good agreement with the experimental measurements. However, at large tilting angles, a small difference can be noted due to the limited accuracy of the setup regarding tilting angle adjustments. Therefore, also FEM simulations have been performed to verify the results of the analytical model. Furthermore, the maximum tilting angle before the system without payload becomes unstable, i.e., the gradient becomes positive, is determined as  $\theta_{y,\max} = 27^\circ$  where a maximum stabilizing torque of  $|T_{y,\min}| = 72.8$  mNm is achieved. The tilting stiffness is again found by the torque gradient at  $\theta_y \rightarrow 0$  which leads to  $dT_y/d\theta_y = -2.5$  mNm/°. Therefore, the performed measurements show that the designed MB achieves the stability type ( $F_z, T_{xy}$ ) for the shown levitation point. Moreover, the same stability type has been observed by performing simulations for each levitation height/payload.

### VIII. CONCLUSIONS

In this paper, a simple analytical method to calculate the 3D magnetic forces and torques between permanent magnets (PMs) is presented. The PMs are first substituted by model coils based on the Ampèrian model, and with a discretization of the Biot-Savart law, the 3D field is calculated. This simply allows calculating all forces and torques of any arbitrary geometry based on the Lorentz law. Furthermore, with the displacement method, stiffnesses in all six degrees of freedom (DOFs) can be determined.

Taking an axially symmetric magnetic bearing (MB) as an example, it is shown that depending on the selected MB dimensions different stability types are obtained, and ring-shaped PMs are outperforming disc-shaped PMs concerning achievable stiffnesses by several orders of magnitudes, however, lead to a slightly reduced axial levitation height. With the performed Pareto optimization it is shown that a characteristic dimension related levitation height (CDRLH) of around 1.5 can be achieved, however, if a minimum payload capacity of 50 times the mover weight and a tilting stiffness of  $dT_y/d\theta_y = 1$  mNm/° are considered, the maximum CDRLH reduces to around 1, which is still almost a factor of two higher as obtained with commercially available products, even with a more stringent constraint on the payload capacity.

Furthermore, the forces calculated with the proposed analytical approach are verified on a 6DOF test setup, which reveals a good matching between calculations and experimental results independent of the chosen number of model windings.

As a final consideration, one can extend the proposed analytic 3D method to any kind of ironless MB, e.g., systems with radially arranged PMs or systems featuring Halbach arrays since in the magnetic flux density and force calculation process no assumptions on the shape or any symmetries are made. In fact, as long as one is able to substitute the PMs in the system with current-carrying coils, arranged such that their magnetic flux density distribution is replicated, the presented discretization and summation process for calculating the magnetic forces can be conducted. With a further deep investigation, in combination with the method of images, the forces in simple MBs employing iron core structures could be calculated. However, in this case, one also has to consider the effort for building the model, its time performance, and precision compared to the commonly used FEM simulations.

### APPENDIX A SCALING LAWS

With the performed Pareto optimization in **Sec. VI**, the optimal dimensions of the PMs were found, which for the defined design space resulted in a calculated maximum levitation height of 123.8 mm and payload capacity of 17.4 kg. If at a later stage, the demanded specifications, e.g., concerning the desired maximum levitation height or the payload would change, one would not have to perform the complete optimization routine again. Instead, the scaling laws derived in this section could be used, which directly allow determining the new PM dimensions, such that the new requirements concerning levitation height, forces, torques, or stiffnesses can be met.

#### A. Proportionality Factors

For the derivation of the scaling laws, proportionality factors ( $k_1$  and  $k_2$ ) between different design variables (stator radius  $r_s$ , mover radius  $r_m$ , and levitation coordinate  $z_h$ , i.e., the vertical distance between the stator's and mover's center of mass) are introduced such that the resulting flux density, forces and torques can be expressed with a reduced number of variables

$$r_m = k_1 r_s \quad (15)$$

$$z_h = k_2 r_s \quad (16)$$

$$|\mathbf{r}| \propto r_s. \quad (17)$$

Furthermore, the equivalent ampèrian current of a PM, given in (1), is directly proportional to the height of the corresponding PM

$$I_i \propto h_i \quad \text{with } i = \{s, m\}. \quad (18)$$

Accordingly, the magnetic flux density  $|\mathbf{B}|$  derived in (4) can be related to the defined quantities as

$$|\mathbf{B}| \propto \frac{I_s \cdot r_s \cdot r_s}{r_s^3} \propto \frac{h_s}{r_s}, \quad (19)$$

which means that the magnetic flux density is directly proportional to the stator thickness and inversely proportional to the stator radius.

Furthermore, from (5) and (19), it follows that the force  $|\mathbf{F}_{\text{tot}}|$  is directly proportional to the thickness of both PMs and to the proportionality constant  $k_1$

$$|\mathbf{F}_{\text{tot}}| \propto \frac{I_m \cdot r_m \cdot h_s}{r_s} \propto h_m h_s k_1, \quad (20)$$

meaning that also the ratio between the PM radii has an impact on the force magnitude.

The torque  $|\mathbf{T}_{\text{tot}}|$  can be characterized by combining (6) and (20) as

$$|\mathbf{T}_{\text{tot}}| \propto r_m h_m h_s k_1 = h_m h_s r_s k_1^2. \quad (21)$$

Finally, the mover's gravitational force  $F_g$ , which is of fundamental importance to determine the levitation height  $h$ , is determined as

$$F_g \propto h_m r_m^2 = h_m r_s^2 k_1^2, \quad (22)$$

which is proportional to the volume of the mover.

### B. Scaling laws

Based on the derived proportionalities between forces, torques and MB size, the dimensions of the already characterized MB can be scaled. There, it is assumed that the original mover radius  $r_m$  and stator radius  $r_s$  are scaled by the same factor  $a_1$  to the new mover radius  $r_m^*$  and stator radius  $r_s^*$  as

$$r_m^* = a_1 r_m \quad (23)$$

$$r_s^* = a_1 r_s. \quad (24)$$

In the general case, where the PMs are ring shaped magnets, both mover's and stator's radii have to be scaled by the same factor  $a_1$ .

The scaling of the PM heights  $h_m$  and  $h_s$  are found under the condition that the axial force, given by  $|\mathbf{F}_{\text{tot}}|$ , scales with the same factor as the gravitational force  $F_g$ . Hence, the original stator height  $h_s$  scales with  $a_1^2$ , whereas for the original mover height  $h_m$  an arbitrary scaling factor  $a_2$  can be selected

$$h_s^* = a_1^2 h_s \quad (25)$$

$$h_m^* = a_2 h_m. \quad (26)$$

Consequently, applying these scaling factors  $a_1$  and  $a_2$  to the force and torque equations given in (20), (21), and (22), it follows for the new forces  $|\mathbf{F}_{\text{tot}}|^*$ ,  $F_g^*$  and torque  $|\mathbf{T}_{\text{tot}}|^*$

$$|\mathbf{F}_{\text{tot}}|^* = a_1^2 a_2 |\mathbf{F}_{\text{tot}}| \quad (27)$$

$$|\mathbf{T}_{\text{tot}}|^* = a_1^3 a_2 |\mathbf{T}_{\text{tot}}| \quad (28)$$

$$F_g^* = a_1^2 a_2 F_g. \quad (29)$$

It can be noted that both force equations scale with the same factor  $a_1^2 a_2$ , whereas the torque even scales with  $a_1^3 a_2$ . Furthermore, based on (16), the original levitation coordinate  $z_h$  scales as

$$z_h^* = a_1 z_h, \quad (30)$$

thus, the new levitation height  $h^*$  is found as

$$h^* = z_h^* - \frac{h_s^*}{2} - \frac{h_m^*}{2} = a_1 z_h - \frac{a_1^2 h_s}{2} - \frac{a_2 h_m}{2} \quad (31)$$

Finally, the force and torque gradients are obtained by deriving (27) and (28) with respect to a small displacement or rotation as

$$\text{grad}(F)^* = a_1 a_2 \cdot \text{grad}(F) \quad (32)$$

$$\text{grad}(T)^* = a_1^3 a_2 \cdot \text{grad}(T). \quad (33)$$

As a simple and useful conclusion of these scaling laws, it can be stated that: if only the mover height  $h_m$  is scaled

**TABLE III:** Dimensions of the scaled optimal geometry of **Tab. I** resulting from the scaling laws.

Mover	Value	Stator	Value
$r_{m,\text{ext}}^*$	81.3 mm	$r_{s,\text{ext}}^*$	62.5 mm
$r_{m,\text{int}}^*$	45 mm	$r_{s,\text{int}}^*$	35 mm
$h_m^*$	9.2 mm	$h_s^*$	32.8 mm
Mag. Direction	Down	Mag. Direction	Up

**TABLE IV:** Characteristics of the scaled optimal geometry of **Tab. II** obtained applying the scaling laws for the case  $N_s = N_m = 10$ . The correctness of the values has been verified with simulations.

Parameter	Value	Factor	Value
$h^*$	150 mm	$a_1$	1.25
CDRLH*	0.923		
$(dF_x/dx)^*$	77.6 N/m	$a_1 a_2$	2.3
$(dF_z/dz)^*$	-151.9 N/m	$a_1 a_2$	2.3
$(dT_y/d\theta_y)^*$	-3.6 mNm/°	$a_1^3 a_2$	3.6
$T_{y,\text{max}}^*$	48.2 mNm	$a_1^3 a_2$	3.6
$\theta_{y,\text{max}}^*$	18°		
$x_{\text{max}}^*$	20 mm	$a_1$	1.25
$F_{z,\text{max}}^*/F_g^*$	55.8		
Mover Mass $m_m^*$	1 kg	$a_1^2 a_2$	2.88
Payload Cap.*	50 kg		

with the factor  $a_2$ , all forces, torques, and corresponding gradients are also scaling linearly with  $a_2$ , whereas the levitation coordinate  $z_h$  remains the same since it only depends on the factor  $a_1$ . Further, if  $a_1$  is increased, the forces and torques even scale with  $a_1^2$  and  $a_1^3$ , respectively.

### C. Example

In the following, to demonstrate the effectiveness of the scaling laws, the optimized MB designed in **Sec. VI** should be scaled to a new MB which achieves a maximum levitation height of  $h = 150$  mm and features a payload capacity of 50 kg.

Based on (31) and (29), the two scaling factors are directly found as  $a_1 = 1.25$  and  $a_2 = 1.84$ . **Tab. III** shows the dimensions of the scaled PMs, and in **Tab. IV** the characteristics of the scaled MB are reported.

### ACKNOWLEDGMENT

The authors are very much indebted to the "Else und Friedrich Hugel-Fonds für Mechatronik / ETH Foundation" which generously supports the exploration of physical limits of magnetically levitated systems at the Power Electronic Systems Laboratory.

### REFERENCES

- [1] A. V. Filatov and E. H. Maslen, "Passive magnetic bearing for flywheel energy storage systems," *IEEE Transactions on Magnetics*, vol. 37, no. 6, pp. 3913–3924, 2001.
- [2] T. Masuzawa, S. Ezoe, T. Kato, and Y. Okada, "Magnetically suspended centrifugal blood pump with an axially levitated motor," *Artificial organs*, vol. 27, no. 7, pp. 631–638, 2003.
- [3] M. Khamesee and E. Shameli, "Regulation technique for a large gap magnetic field for 3D non-contact manipulation," *Mechatronics*, vol. 15, no. 9, pp. 1073 – 1087, 2005.
- [4] G. Jansen, "Magnetic levitation apparatus," International Patent WO 2009/038 464 A2, Mar 26, 2009.
- [5] X. Wang and L. Li, "Magnetic suspension device," U.S. Patent US 8,294,542 B2, Oct 23, 2012.
- [6] J.-P. Yonnet, "Permanent magnet bearings and couplings," *IEEE Transactions on Magnetics*, vol. 17, no. 1, pp. 1169–1173, 1981.
- [7] G. Akoun and J.-P. Yonnet, "3D analytical calculation of the forces exerted between two cuboidal magnets," *IEEE Transactions on magnetics*, vol. 20, no. 5, pp. 1962–1964, 1984.
- [8] E. Furlani, "A formula for the levitation force between magnetic disks," *IEEE Transactions on Magnetics*, vol. 29, no. 6, pp. 4165–4169, 1993.

- [9] R. Ravaut, G. Lemarquand, V. Lemarquand, and C. Depollier, "Analytical calculation of the magnetic field created by permanent-magnet rings," *IEEE Transactions on Magnetics*, vol. 44, no. 8, pp. 1982–1989, Aug 2008.
- [10] S. I. Babic and C. Akyel, "Improvement in the analytical calculation of the magnetic field produced by permanent magnet rings," *Progress In Electromagnetics Research*, vol. 5, pp. 71–82, 2008.
- [11] R. Ravaut, G. Lemarquand, and V. Lemarquand, "Force and stiffness of passive magnetic bearings using permanent magnets. part 1: Axial magnetization," *IEEE transactions on magnetics*, vol. 45, no. 7, pp. 2996–3002, 2009.
- [12] —, "Force and stiffness of passive magnetic bearings using permanent magnets. part 2: Radial magnetization," *IEEE Transactions on Magnetics*, vol. 45, no. 9, pp. 3334–3342, 2009.
- [13] W. Robertson, B. Cazzolato, and A. Zander, "A simplified force equation for coaxial cylindrical magnets and thin coils," *IEEE Transactions on magnetics*, vol. 47, no. 8, pp. 2045–2049, 2011.
- [14] S. Babic, C. Akyel, J. Martinez, and B. Babic, "A new formula for calculating the magnetic force between two coaxial thick circular coils with rectangular cross-section," *Journal of Electromagnetic Waves and Applications*, vol. 29, no. 9, pp. 1181–1193, 2015.
- [15] H. Qin, Z. Ming, T. Wen, and Y. Zhao, "Force calculation for hybrid magnetic levitation system," in *2018 14th International Conference on Computational Intelligence and Security (CIS)*, Nov 2018, pp. 88–92.
- [16] M. Lahdo, T. Stroehla, and S. Kovalev, "Semi-analytical 3D force calculation of an ironless cylindrical permanent magnet actuator for magnetic levitation systems," *ACES*, vol. 34, no. 4, pp. 520–527, Apr 2019.
- [17] M.-S. Sim and J.-S. Ro, "Semi-analytical modeling and analysis of halbach array," *Energies*, vol. 13, no. 5, pp. 1252–1262, Mar 2020.
- [18] Tecnotion, "UM series ironless," *Power*, vol. 5, pp. 5–55, 2011.
- [19] R. F. Post, T. K. Fowler, and S. F. Post, "A high-efficiency electromechanical battery," *Proceedings of the IEEE*, vol. 81, no. 3, pp. 462–474, 1993.
- [20] E. P. Furlani, *Permanent magnet and electromechanical devices: materials, analysis, and applications*. Academic press, 2001.
- [21] G. Jungmayr, E. Marth, W. Amrhein, H.-J. Berroth, and F. Jeske, "Analytical stiffness calculation for permanent magnetic bearings with soft magnetic materials," *IEEE Transactions on Magnetics*, vol. 50, no. 8, pp. 1–8, 2014.
- [22] J. Janssen, J. Paulides, L. Encica, and E. Lomonova, "Analytical modeling of permanent magnets on a soft magnetic support for a suspension system," in *2008 International Conference on Electrical Machines and Systems*. IEEE, 2008, pp. 3825–3830.
- [23] S. Earnshaw, "On the nature of the molecular forces which regulate the constitution of the luminiferous ether," *Transactions of the Cambridge Philosophical Society*, vol. 7, pp. 97–112, 1848.
- [24] A. Bettini, *A Course in Classical Physics 3–Electromagnetism*. Springer, 2016, p. 301.
- [25] A. E. Fitzgerald, C. Kingsley, S. D. Umans, and B. James, *Electric machinery*. McGraw-Hill New York, 2003, vol. 5, pp. 4 & 30.
- [26] S. Babic and C. Akyel, "Magnetic force between inclined circular filaments placed in any desired position," *IEEE transactions on magnetics*, vol. 48, no. 1, pp. 69–80, 2011.
- [27] K.-B. Kim, E. Levi, Z. Zabar, and L. Birenbaum, "Restoring force between two noncoaxial circular coils," *IEEE Transactions on Magnetics*, vol. 32, no. 2, pp. 478–484, 1996.
- [28] —, "Mutual inductance of noncoaxial circular coils with constant current density," *IEEE transactions on magnetics*, vol. 33, no. 5, pp. 4303–4309, 1997.
- [29] H. A. Haus and J. R. Melcher, *Electromagnetic fields and energy*. Prentice Hall Englewood Cliffs, NJ, 1989, vol. 107.



**Reto Bonetti** received his B.Sc. and M.Sc. degree in Electrical Engineering and Information Technology at the Swiss Federal Institute of Technology (ETH) in Zurich in 2018 and 2020, respectively, where he focused on power electronics, electrical drive systems, as well as control theory. In August 2020, he joined the Power Electronics Systems Laboratory of ETH Zurich as a Ph.D. student, where he is working on active magnetic bearings featuring large air gaps with integrated wireless power transfer.



**Dominik Bortis** received the M.Sc. and Ph.D. degree in electrical engineering from the Swiss Federal Institute of Technology (ETH) Zurich, Switzerland, in 2005 and 2008, respectively. In May 2005, he joined the Power Electronic Systems Laboratory (PES), ETH Zurich, as a Ph.D. student. From 2008 to 2011, he has been a Postdoctoral Fellow and from 2011 to 2016 a Research Associate with PES, cosupervising Ph.D. students and leading industry research projects. Since January 2016 Dr. Bortis is heading the research group Advanced Mechatronic Systems at PES, which concentrates on ultra-high speed motors, magnetic bearings and bearingless drives, new linear-rotary actuator and machine concepts with integrated power electronics. Targeted applications include e.g. highly dynamic and precise positioning systems, medical and pharmaceutical systems, and future mobility concepts. Dr. Bortis has published 90+ scientific papers in international journals and conference proceedings. He has filed 30+ patents and has received 7 IEEE Conference Prize Paper Awards and 1 First Prize Transaction Paper Award.



**Lars Beglinger** received both the B.Sc. degree in Mechanical Engineering and the M.Sc. degree in Micro- and Nanosystems from the Swiss Federal Institute of Technology (ETH) in Zurich in 2018 and 2021, respectively. For his master thesis, he was working on the implementation of a high robustness force sensor concept to determine the position of a levitating magnet with high positional resolution at the Power Electronic Systems Laboratory of ETH Zurich. His research interests include novel electromechanical sensors and transducers.



**Dr. Johann W. Kolar** is a Fellow of the IEEE and is currently a Full Professor and the Head of the Power Electronic Systems Laboratory at the Swiss Federal Institute of Technology (ETH) Zurich. He has proposed numerous novel converter concepts incl. the Vienna Rectifier, the Sparse Matrix Converter and the Swiss Rectifier, has spearheaded the development of x-million rpm motors, and has pioneered fully automated multi-objective power electronics design procedures. He has graduated 75+ Ph.D. students, has published 900+ journal and conference papers and 4 book chapters, and has filed 200+ patents. He has presented 30+ educational seminars at leading inter-national conferences and has served as IEEE PELS Distinguished Lecturer from 2012 2016. He has received 35+ IEEE Transactions and Conference Prize Paper Awards, the 2014 IEEE Power Electronics Society R. David Middlebrook Achievement Award, the 2016 IEEE PEMC Council Award, the 2016 IEEE William E. Newell Power Electronics Award, and two ETH Zurich Golden Owl Awards for excellence in teaching. He was elected to the U.S. National Academy of Engineering as an international member in 2021. The focus of his current research is on ultra-compact/efficient WBG converter systems, ANN-based design procedures, Solid-State Transformers, ultra-high speed drives, and bearingless motors.